# Supplementary information for 'Broadband ultrafast self-heterodyned chiro-optical spectroscopy'

Francesco Gucci[1†], Andrea Iudica[1†], Andres Valladares Y Tacchi[1†], Andrea Schirato[1,2], Giulia Crotti[1], Ryeong Myeong Kim[3], Soo Min Lee[3], Jeong Hyun Han[3], Andrea Villa[1], Dawar Ali[4,5], Aurora Rizzo[4], Margherita Maiuri[1], Ki Tae Nam[3], Giuseppe Della Valle[1], Giulio Cerullo[1,6*]

[1]Dipartimento di Fisica, Politecnico di Milano, Piazza Leonardo da Vinci 32, Milano, 20133, Italy.
[2]Department of Physics and Astronomy, Rice University, 6100 Main St, Houston, Texas, 77005, United States.
[3]Department of Materials Science and Engineering, Seoul National University, Seoul, Republic of Korea.
[4]CNR NANOTEC, Istituto di Nanotecnologia, c/o Campus Ecotekne, Via Monteroni, Lecce, 73100, Italy.
[5]Università del Salento, Via Monteroni, Lecce, 73100, Italy.
[6]CNR-IFN, Piazza Leonardo da Vinci 32, Milano, 20133, Italy.

Corresponding author: giulio.cerullo@polimi.it;
[†]These authors contributed equally to this work.

# Supplementary Note 1: Analytical derivation of the static and transient chiro-optical susceptibility from the experimental interferograms

In an isotropic chiral medium, the polarization $\mathbf{P}$ is given by the following constitutive relation [1]:

$$\mathbf{P} = \varepsilon_0 \chi_{\text{achi}} \mathbf{E} + \mathrm{i}\sqrt{\mu_0 \varepsilon_0}\chi_{\text{chi}} \mathbf{H}, \tag{1}$$

with $\varepsilon_0$, $\mu_0$ the vacuum permittivity and permeability, respectively. For a linearly polarized electromagnetic wave propagating in a chiral medium, the polarization vector will comprise two components, i.e. an achiral component (parallel to the incoming field), and a chiral one, parallel to the magnetic field, hence orthogonal to the incoming electric field. In other words, chiral light matter interactions arise from the coupling of electric and magnetic dipole moments [2].

When using the $\exp(\mathrm{i}\omega t)$ sign convention for the phase of time-harmonic fields, the frequency-domain wave equation associated to such medium is expressed as follows:

$$\nabla^2 \mathbf{E} + 2\omega\chi_{\text{chi}}\sqrt{\varepsilon_0 \mu_0}(\nabla \times \mathbf{E}) + \omega^2 \mu \varepsilon \mathbf{E} = 0, \tag{2}$$

having defined the material permittivity and permeability $\varepsilon = \varepsilon_0 \varepsilon_r$ and $\mu = \mu_0 \mu_r$.

This equation admits two eigensolutions, in the form of left (LCP) and right circularly-polarized (RCP) plane waves, having different propagation constants [3]. The LCP and RCP light will thus have different complex-valued refractive indices, respectively $\tilde{n}_{\text{LCP}}$, $\tilde{n}_{\text{RCP}}$:

$$\begin{aligned} \tilde{n}_{\text{LCP}} &= \sqrt{\mu_r \varepsilon_r} + \chi_{\text{chi}}, \\ \tilde{n}_{\text{RCP}} &= \sqrt{\mu_r \varepsilon_r} - \chi_{\text{chi}} \end{aligned} \tag{3}$$

so that the difference $\Delta\tilde{n} = \tilde{n}_{\text{LCP}} - \tilde{n}_{\text{RCP}}$ is simply:

$$\Delta\tilde{n} = 2\chi_{\text{chi}}. \tag{4}$$

Since $\tilde{n}_{\text{LCP,RCP}}$ act as complex-valued refractive indices for light with opposing helicities, $\mathrm{Re}(\tilde{n}_{\text{LCP,RCP}}) =: n_{\text{LCP,RCP}}$ and $\mathrm{Im}(\tilde{n}_{\text{LCP,RCP}}) =: \kappa_{\text{LCP,RCP}}$ are related to the dispersion and absorption of LCP and RCP waves within the chiral medium. Thus, $\Delta\tilde{n}$ is a measure of the difference in phase shift and absorption of LCP and RCP light. For light with angular frequency $\omega$, upon propagation in a chiral medium of length $L$, the optical activity is defined as:

$$\mathrm{ORD} + \mathrm{iCD} = \frac{\omega L}{2c}\Delta\tilde{n} = \frac{\omega L}{c}\chi_{\text{chi}}, \tag{5}$$

with $c$ the speed of light. Here the real part of the optical activity (i.e., the optical rotatory dispersion, ORD) corresponds to the total angular rotation of the polarization direction of light after propagating within the medium, while the imaginary part (i.e., the circular dichroism, CD) gives the difference in absorbance of LCP and RCP light

[2]. This is equivalent to the following definitions of CD, ORD:

$$\mathrm{CD} = \frac{\ln(10)}{4}\left(\alpha_{\mathrm{LCP}} - \alpha_{\mathrm{RCP}}\right), \tag{6}$$

$$\mathrm{ORD} = \frac{L\omega}{2c}\left(n_{\mathrm{LCP}} - n_{\mathrm{RCP}}\right), \tag{7}$$

with $\alpha_{\mathrm{LCP,RCP}}$ the absorbances.

Hereafter, since $\chi_{\mathrm{chi}} \propto \mathrm{ORD} + \mathrm{iCD}$, we will make use of the following definition of the chiro-optical susceptibility, ignoring the prefactor:

$$\chi^0_{\mathrm{chi}} := \mathrm{ORD} + \mathrm{iCD} = \frac{\omega L}{c}\chi_{\mathrm{chi}}. \tag{8}$$

Extracting CD, ORD and their dynamic counterparts can be understood through a Jones matrix analysis of the polarization state of the probe beam in our setup. We use the following sign convention for the phase of a monochromatic plane wave of angular frequency $\omega$, propagating along the direction defined by the wave vector $\mathbf{k}$ (refer to Fig. S1):

$$\exp\left[\mathrm{i}\left(\omega t - \mathbf{kr}\right)\right].$$

In the calculations hereafter, we will omit this total phase term for the sake of conciseness. The sign convention for the circular basis of the Jones vectors used in this work is shown in Fig. S1.

The Glan Taylor prism polarizes the beam along the vertical axis. Thus, the field of a monochromatic plane wave of angular frequency $\omega$ and complex amplitude $E_0(\omega)$, can be written, after the prism, as:

$$E_1(\omega) = E_0(\omega)\begin{bmatrix}0\\1\end{bmatrix}. \tag{9}$$

Subsequently, the interaction with the chiral sample takes place. The sample mean absorbance and refractive index are defined respectively as:

$$\alpha = \left(\alpha_{\mathrm{LCP}} + \alpha_{\mathrm{RCP}}\right)/2,$$
$$n = \left(n_{\mathrm{LCP}} + n_{\mathrm{RCP}}\right)/2,$$

with $\alpha_{\mathrm{LCP,RCP}}$, $n_{\mathrm{LCP,RCP}}$ as before.

We write the Jones matrix associated with an optically active sample as follows (within the limit of weak ORD and CD):

$$M_{\mathrm{chi}} \approx 10^{-\alpha/2}\mathrm{e}^{-\mathrm{i}\rho}\begin{bmatrix}1 & \mathrm{ORD} - \mathrm{iCD}\\ -\mathrm{ORD} + \mathrm{iCD} & 1\end{bmatrix}, \tag{10}$$

where $\rho = nL\omega/c$.

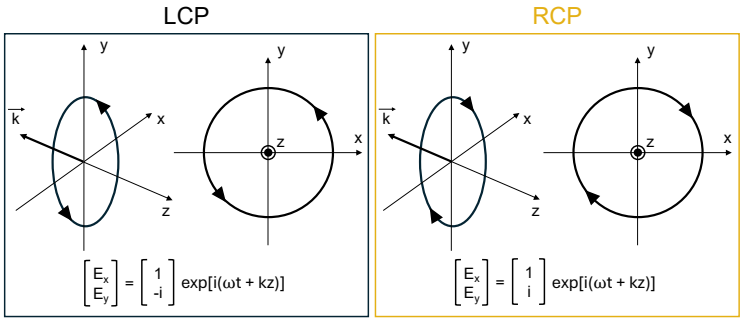


**Fig. S1 Scheme of the Jones vector circular basis.** Illustration of the convention used in the analytical and numerical derivations of CD and ORD. The schematic depicts the polarization state of light corresponding to a specific Jones vector, assuming a planewave propagating along the $-z$ direction, either left-circularly polarized (left panel) and right-circularly polarized (right panel) light.

Thus, the field transmitted after interaction with the sample will contain a small polarization rotation, an intrinsic change in ellipticity (quantified by ORD and CD, respectively), and a change in amplitude due to absorption:

$$E_2(\omega) = M_{\text{chi}} E_1(\omega) = 10^{-\alpha/2} \mathrm{e}^{-\mathrm{i}\rho} E_0(\omega) \begin{bmatrix} \text{ORD} - \text{iCD} \\ 1 \end{bmatrix}. \tag{11}$$

Notice that the two components $E_{2x}(\omega)$ and $E_{2y}(\omega)$ above correspond to the Fourier transforms of $E_{\text{CFID}}(t)$ and $E_{\text{AFID}}(t)$ respectively, consistent with the definitions in Fig. 1 in the main text:

$$\tilde{E}_{\text{CFID}}(\omega) := \text{FT}[E_{\text{CFID}}(t)] = E_{2x}(\omega),$$
$$\tilde{E}_{\text{AFID}}(\omega) := \text{FT}[E_{\text{AFID}}(t)] = E_{2y}(\omega).$$

The common-path interferometer (CPI) introduces a variable delay $\tau$ between the chiral free induction decay (CFID) and achiral free induction decay (AFID), which can be treated as a phase term between the vertical and horizontal components of the electric field ($\phi = \omega\tau$).

$$E_3(\omega, \tau) = 10^{-\alpha/2} \mathrm{e}^{-\mathrm{i}\rho} E_0(\omega) \begin{bmatrix} \text{ORD} - \text{iCD} \\ \mathrm{e}^{\mathrm{i}\phi} \end{bmatrix}. \tag{12}$$

The Wollaston prism is treated as a set of two polarizers oriented at $\pm 45°$ with respect to the vertical. The polarization state at the two photodiodes ($E_4^{\pm}$, respectively) can be expressed as:

$$\begin{aligned} E_4^{+}(\omega, \tau) &= \frac{1}{2} \begin{bmatrix} 1 & 1 \\ 1 & 1 \end{bmatrix} E_3(\omega, \tau) = \frac{1}{2} \cdot 10^{-\alpha/2} \mathrm{e}^{-\mathrm{i}\rho} E_0(\omega) \begin{bmatrix} \text{ORD} - \text{iCD} + \mathrm{e}^{\mathrm{i}\phi} \\ \text{ORD} - \text{iCD} + \mathrm{e}^{\mathrm{i}\phi} \end{bmatrix}, \\ E_4^{-}(\omega, \tau) &= \frac{1}{2} \begin{bmatrix} 1 & -1 \\ -1 & 1 \end{bmatrix} E_3(\omega, \tau) = \frac{1}{2} \cdot 10^{-\alpha/2} \mathrm{e}^{-\mathrm{i}\rho} E_0(\omega) \begin{bmatrix} \text{ORD} - \text{iCD} - \mathrm{e}^{\mathrm{i}\phi} \\ -\text{ORD} + \text{iCD} + \mathrm{e}^{\mathrm{i}\phi} \end{bmatrix}. \end{aligned} \tag{13}$$

The corresponding intensities are, up to first order in CD and ORD:

$$I_4^+(\omega,\tau) = \left(\frac{c\varepsilon_0}{2}\right) \cdot \frac{1}{2} \cdot 10^{-\alpha} \left|E_0(\omega)\right|^2 (1 + 2\mathrm{ORD}\cos\phi - 2\mathrm{CD}\sin\phi)\,,$$
$$I_4^-(\omega,\tau) = \left(\frac{c\varepsilon_0}{2}\right) \cdot \frac{1}{2} \cdot 10^{-\alpha} \left|E_0(\omega)\right|^2 (1 - 2\mathrm{ORD}\cos\phi + 2\mathrm{CD}\sin\phi)\,.$$

By integrating intensities of the two fields over all frequencies $\omega$ of the probe, and by taking the difference between them, we obtain a complete expression for the chiral interferogram, $U_{\mathrm{chi}}(\tau)$, expressed in terms of the initial field amplitude $E_0(\omega)$, and the sample-specific CD and ORD:

$$U_{\mathrm{chi}}(\tau) = I_4^+(\tau) - I_4^-(\tau) = \left(\frac{c\varepsilon_0}{2}\right) 2 \int \mathrm{d}\omega \left|E_0(\omega)\right|^2 10^{-\alpha(\omega)} [\mathrm{ORD}\cos(\omega\tau) - \mathrm{CD}\sin(\omega\tau)]. \tag{14}$$

The Fourier transform $\tilde{U}_{\mathrm{chi}}(\omega)$ of $U_{\mathrm{chi}}(\tau)$ is[1]

$$\tilde{U}_{\mathrm{chi}}(\omega) := \mathrm{FT}[(U_{\mathrm{chi}}(\tau)] = \left(\frac{c\varepsilon_0}{2}\right) \left|E_0(\omega)\right|^2 10^{-\alpha(\omega)} (\mathrm{ORD} + \mathrm{iCD}) \propto \chi_{\mathrm{chi}}.$$

Notice also that

$$\tilde{U}_{\mathrm{chi}}(\omega) = \left(\frac{c\varepsilon_0}{2}\right) E_{2x}^*(\omega) E_{2y}(\omega) = \left(\frac{c\varepsilon_0}{2}\right) \tilde{E}_{\mathrm{CFID}}^*(\omega) \tilde{E}_{\mathrm{AFID}}(\omega). \tag{15}$$

In order to isolate the chiro-optical properties (namely, ORD, CD) of the sample, a calibration interferogram is taken, this time by setting the probe polarization at 45° with respect to the horizontal axis. Using Jones calculus again, up to order zero in CD and ORD[2], it can be shown that

$$U_{\mathrm{achi}}(\tau) = \left(\frac{c\varepsilon_0}{2}\right) \int \mathrm{d}\omega \left|E_0(\omega)\right|^2 10^{-\alpha(\omega)} \cos(\omega\tau), \tag{16}$$

whose Fourier transform is

$$\tilde{U}_{\mathrm{achi}}(\omega) := \mathrm{FT}[U_{\mathrm{achi}}(\tau)] = \left(\frac{c\varepsilon_0}{2}\right) \frac{1}{2} |E_0(\omega)|^2 10^{-\alpha(\omega)}. \tag{17}$$

Notice also that

$$\tilde{U}_{\mathrm{achi}}(\omega) = \left(\frac{c\varepsilon_0}{2}\right) \frac{1}{2} \tilde{E}_{\mathrm{AFID}}^*(\omega) \tilde{E}_{\mathrm{AFID}}(\omega). \tag{18}$$

The full chiro-optical susceptibility is thus retrieved by taking the ratio of the Fourier-transformed interferograms:

$$\chi_{\mathrm{chi}}^0 = \frac{1}{2} \frac{\tilde{U}_{\mathrm{chi}}(\omega)}{\tilde{U}_{\mathrm{achi}}(\omega)}, \tag{19}$$

[1] Notice that we are using the following definition of Fourier transform, consistent with our sign convention for the phasors: $\tilde{f}(\omega) = \mathrm{FT}[f(\tau)] = \int \mathrm{d}\tau f(\tau) \exp(-\mathrm{i}\omega\tau)$.

[2] Here, we neglect terms $O(CD)$, $O(ORD)$, since we need $\tilde{U}_{\mathrm{Achi}}(\omega)$ as a normalization integral, to obtain the following expressions to first order in CD, ORD.

and

$$\begin{aligned} \mathrm{CD}(\omega) &= \frac{1}{2}\,\mathrm{Im}\left[\frac{\tilde{U}_{\mathrm{chi}}(\omega)}{\tilde{U}_{\mathrm{achi}}(\omega)}\right], \\ \mathrm{ORD}(\omega) &= \frac{1}{2}\,\mathrm{Re}\left[\frac{\tilde{U}_{\mathrm{chi}}(\omega)}{\tilde{U}_{\mathrm{achi}}(\omega)}\right]. \end{aligned} \tag{20}$$

A complementary way of treating the setup in the time domain is to consider the interference of the CFID and AFID directly, whose relative delay is controlled by the CPI. The setup is based on FT time-domain interferometry, which measures either autocorrelation or cross-correlation signals by controlling the time delay between the achiral and chiral fields. When acquiring the chiral interferogram, the total readout of each photodiode $I_{\pm}$ at a given CPI delay $\tau$ is given by:

$$\begin{aligned} I_{\pm}(\tau) &\propto \int_{-\infty}^{+\infty} \mathrm{d}t\, |E_{\mathrm{CFID}}\,(t) \pm E_{\mathrm{AFID}}\,(t+\tau)|^2 \\ &\propto \int_{-\infty}^{+\infty} \mathrm{d}t\, |E_{\mathrm{CFID}}\,(t)|^2 + \int_{-\infty}^{+\infty} \mathrm{d}t\, |E_{\mathrm{AFID}}\,(t+\tau)|^2 \\ &\quad \pm 2 \times \mathrm{Re} \int_{-\infty}^{+\infty} \mathrm{d}t E_{\mathrm{CFID}}\,(t) E^*_{\mathrm{AFID}}\,(t+\tau), \end{aligned} \tag{21}$$

where it is clear that the last component corresponds to the self-heterodyned signal, having $E_{\mathrm{AFID}}$ as a local oscillator (LO) field. The remaining part is dominated by the autocorrelation signal of the LO. Since we record the differential signal on the two photodiodes, we directly access the heterodyned signal, i.e. the chiral interferogram $U_{\mathrm{Chi}}(\tau)$:

$$U_{\mathrm{chi}}(\tau) = I_+ - I_- \propto \mathrm{Re} \int_{-\infty}^{+\infty} \mathrm{d}t E_{\mathrm{CFID}}(t) E^*_{\mathrm{AFID}}(t+\tau). \tag{22}$$

We now manipulate this expression in order to simplify the calculation of its Fourier transform. We first write

$$U_{\mathrm{chi}}(\tau) \propto \int_{-\infty}^{+\infty} \mathrm{d}t \left[E_{\mathrm{CFID}}(t) E^*_{\mathrm{AFID}}(t+\tau) + E^*_{\mathrm{CFID}}(t) E_{\mathrm{AFID}}(t+\tau)\right]. \tag{23}$$

Then we express $E_{\mathrm{CFID}}(t)$, $E_{\mathrm{AFID}}(t+\tau)$ and their complex conjugates as their Fourier integrals:

$$\begin{aligned} E_{\mathrm{CFID}}(t) &\propto \int \mathrm{d}\omega' \tilde{E}_{\mathrm{CFID}}(\omega') e^{\mathrm{i}\omega' t}, \\ E^*_{\mathrm{CFID}}(t) &\propto \int \mathrm{d}\omega' \tilde{E}^*_{\mathrm{CFID}}(\omega') e^{-\mathrm{i}\omega' t}, \\ E_{\mathrm{AFID}}(t+\tau) &\propto \int \mathrm{d}\omega' \tilde{E}_{\mathrm{AFID}}(\omega') e^{\mathrm{i}\omega'(t+\tau)}, \\ E^*_{\mathrm{AFID}}(t+\tau) &\propto \int \mathrm{d}\omega' \tilde{E}^*_{\mathrm{AFID}}(\omega') e^{-\mathrm{i}\omega'(t+\tau)}, \end{aligned}$$

where the proportional sign $\propto$ accounts for neglecting normalization factors. Substituting these expressions into Eq. (23) and integrating over $t$, one obtains:

$$
\begin{aligned}
U_{\mathrm{chi}}(\tau) &\propto \\
&\propto \iint \mathrm{d}\omega' \mathrm{d}\omega \left[ \tilde{E}_{\mathrm{CFID}}(\omega') \tilde{E}^*_{\mathrm{AFID}}(\omega) e^{-\mathrm{i}\omega\tau} + \tilde{E}^*_{\mathrm{CFID}}(\omega') \tilde{E}_{\mathrm{AFID}}(\omega) e^{\mathrm{i}\omega\tau} \right] \delta(\omega' - \omega) \\
&= \int \mathrm{d}\omega' \tilde{E}_{\mathrm{CFID}}(\omega') \tilde{E}^*_{\mathrm{AFID}}(\omega') e^{-\mathrm{i}\omega'\tau} + \int \mathrm{d}\omega' \tilde{E}^*_{\mathrm{CFID}}(\omega') \tilde{E}_{\mathrm{AFID}}(\omega') e^{\mathrm{i}\omega'\tau}.
\end{aligned}
$$

Now it is straightforward to Fourier transform this expression to obtain $\tilde{U}_{\mathrm{chi}}(\omega)$: for positive frequencies $\omega$, the first integral vanishes, and

$$\tilde{U}_{\mathrm{chi}}(\omega) \propto \tilde{E}^*_{\mathrm{CFID}}(\omega) \tilde{E}_{\mathrm{AFID}}(\omega),$$

which is again Eq. (15). On the other hand, by Fourier-transforming $U_{\mathrm{Achi}}(\tau)$ (with the assumption of small dichroism) we obtain

$$\tilde{U}_{\mathrm{achi}}(\omega) \propto \tilde{E}_{\mathrm{AFID}}(\omega) \tilde{E}^*_{\mathrm{AFID}}(\omega),$$

i.e., Eq. (18). We thus see that the two approaches are fully consistent.

During pump-probe measurements, by demodulating the signal from the balanced photodiodes at the pump frequency (50 kHz), we get access to the differential chiral interferogram, defined as:

$$\Delta U_{\mathrm{chi}}(\tau, \tau_{\mathrm{pp}}) = U^{\mathrm{ON}}_{\mathrm{chi}}(\tau, \tau_{\mathrm{pp}}) - U^{\mathrm{OFF}}_{\mathrm{chi}}(\tau), \tag{24}$$

where $U^{\mathrm{ON}}_{\mathrm{chi}}$ is the chiral interferogram when the pump interacts with the sample, while $U^{\mathrm{OFF}}_{\mathrm{chi}}$ is the same quantity when the pump is off, and corresponds to the aforementioned $U_{\mathrm{chi}}$. $\tau$ and $\tau_{\mathrm{pp}}$ refer respectively to the interferometric delay introduced by the birefringent interferometer and to the pump-probe delay. By performing the measurement for different $\tau_{\mathrm{pp}}$, we obtain a 2D-dataset. We Fourier-transform with respect to the $\tau$-axis, obtaining $\Delta\tilde{U}_{\mathrm{chi}}(\omega, \tau_{\mathrm{pp}})$. After normalization with respect to $\tilde{U}_{\mathrm{achi}}$, in the limit of small pump-induced changes in the transmission spectrum, we get direct access to the transient chiro-optical susceptibility. By taking the real and imaginary parts, we obtain the broadband, transient optical rotatory dispersion ($\Delta\mathrm{ORD}(\omega, \tau_{\mathrm{pp}})$) and circular dichroism ($\Delta\mathrm{CD}(\omega, \tau_{\mathrm{pp}})$) respectively.

## Supplementary Note 2: Sensitivity

The exceptional sensitivity and high throughput of our experimental setup allow us to record transient CD and ORD spectra in the mdeg level in few seconds. Figure S2 shows the $\Delta$CD and $\Delta$ORD recorded on the gold nano-helicoids array for a pump-probe delay $\tau$=100 ps. The shown spectra span a range of $\sim$15 mdeg and were recorded in 84 s (6 second for every spectrum averaged over 14 acquisitions). The shaded areas in the figure depict the standard deviation ($\pm\sigma$) evaluated at negative delays, showcasing

$\sigma$ <1 mdeg over the whole wavelength range shown, with values reaching <400$\mu$deg from ∼630-740 nm.

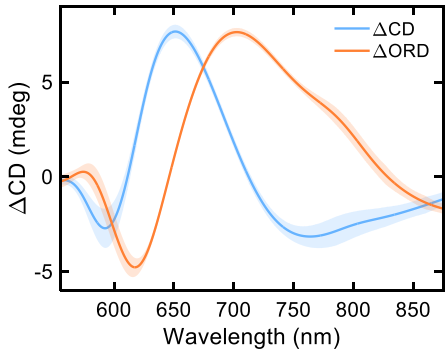


**Fig. S2 Standard deviation of transient CD and ORD spectra.** The solid line show the transient CD and ORD spectra measured on the gold nano-particles array for $\tau$=100 ps. The shaded area represent the standard deviation ($\pm\sigma$) extracted from the data at negative pump-probe delays. The transient spectra were acquired in 84 seconds (6 seconds per spectrum, 14 averages).

In order to characterize the best achievable sensitivity, we performed additional measurements, progressively lowering the pump power (Figure S3, panels a to c). We detected ΔCD and ΔORD at $\tau$=100 ps, successfully recording tens-of-microdegrees signals over a broad spectral range.

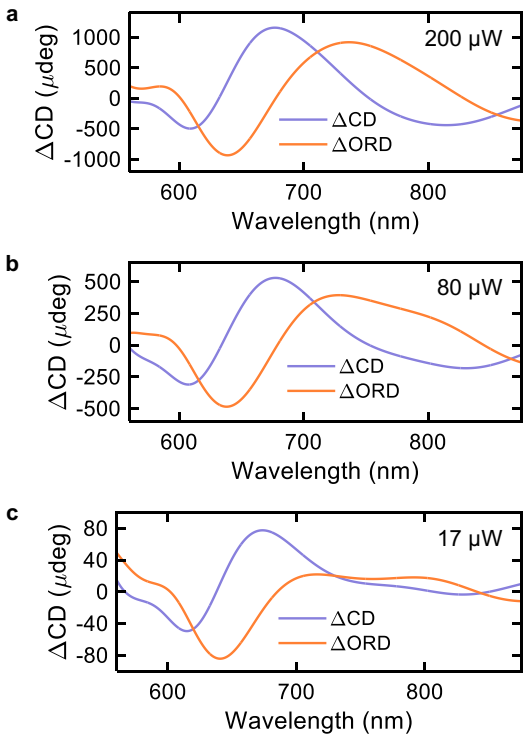


**Fig. S3 Sensitivity measurements.** Transient CD and ORD spectra recorded at pump-probe delay $\tau$=100 ps for different average powers. **a** 200 $\mu$W. **b** 80 $\mu$W. **a** 17 $\mu$W. The $\Delta$CD and $\Delta$ORD spectra at 200 $\mu$W (a) were acquired in five minutes, the ones at 80 $\mu$W in 33 minutes and the ones at 17 $\mu$W in 3 hours. All the experiments shown in this figure were performed on the gold helicoids sample.

## Supplementary Note 3: Measured static chiro-optical response of plasmonic helicoids

Our experimental setup is able to precisely record both the static and dynamic CD and ORD. To benchmark such capability, we perform steady state measurements of the gold nanoparticles array CD and we compare the results with analogous results obtained with a commercially available setup. Figure S4 shows the results. The measurements performed with our setup show that the CD peak central wavelength and shape has a strong dependence on the position on the sample. By repeating the same measurement on three different spots (light orange thin lines in Fig. S4), we observe rather different profiles. Such dependence on the position is due to the heterogeneous orientation of the nanohelicoids over micro-metric lengths, sensitively detected by our 100 $\mu$m-sized probe.

The commercial setup (J-1000, JASCO) we employ to record the static CD follows a typical configuration. The input light polarization state is alternatively switched from circular right to circular left by a photoelastic modulator (PEM) and filtered in energy

by a monochromator. After passing through the sample, it impinges on a detector. The difference in intensity for the two polarization states is measured for different wavelengths, providing the broadband CD response. The beam size is approximately 5 mm $\times$ 5 mm, which effectively covers the full area of the sample. Therefore, the recorded CD spectrum (black thick line in Fig. S4) can be considered as an average over the entire sample surface.

To enable a proper comparison, we average the three local measurements obtained with our experimental setup. The resulting trace shows good agreement with the measurement from the JASCO instrument, confirming the validity of our approach. The differences can be attributed once again to the inhomogeneity of the sample, and the use of a local probe (having a spot size of 100 $\mu$m approximately). We want to highlight that the J-1000 CD spectrometer acquisition time is approximately 2 minutes, while our setup requires only a few seconds ($\sim$6 s), which makes the measurement more than one order of magnitude faster.

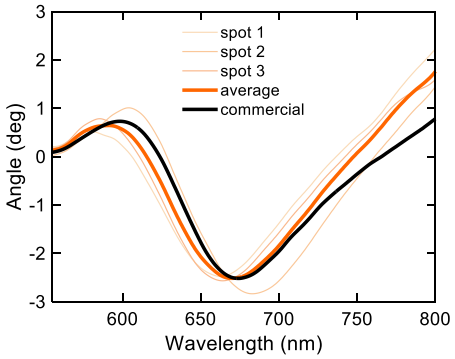


**Fig. S4 Benchmarking of the measured static CD of the nanoparticle array.** Thin orange lines: static CD data measured with the approach presented in the main text, in three different regions of the samples. Thick orange line: average of the static CD spectra taken in spots 1,2,3. Thick black line: Static CD spectrum of the nanoparticle array, acquired via a commercial CD spectrometer (PEM+monochromator), over a large illuminated area ($\sim$ 5x5 mm$^2$).

## Supplementary Note 4: Simulated static chiro-optical response of plasmonic helicoids

To gain further insights into the chiro-optical response of the plasmonic nano-helicoids, we performed additional full-wave electromagnetic simulations using COMSOL Multiphyisics. In these simulations, we modeled an individual Au helicoid in the scattering formalism, namely we treated it as a single, isolated scatterer, embedded in a homogeneous medium. In particular, the nanostructure was placed at the center of a spherical domain of refractive index 1.5 (i.e., the value used for the substrate in the simulations of the nanoparticle array presented in the main text), enclosed within perfectly matched layers. The nanoparticle was illuminated with a monochromatic planewave linearly polarized along the $x$-axis and propagating in the $-z$ direction. The static

metal permittivity was modelled following the same approach discussed in the Methods section of the main text. The vector electric dipole (ED) $\mathbf{p}$, magnetic dipole (MD) $\mathbf{m}$, electric quadrupole (EQ) $\mathbf{Q^e}$ and magnetic quadrupole (MQ) $\mathbf{Q^m}$ moments were computed according to the following expressions [4]:

$$p_\alpha = -\frac{1}{\mathrm{i}\omega}\left\{\int \mathrm{d}^3\mathbf{r}\; J^\omega_\alpha\, j_0(kr) + \frac{k^2}{2}\int \mathrm{d}^3\mathbf{r}\;\left[\,3(\mathbf{r}\cdot\mathbf{J}_\omega)\, r_\alpha - r^2 J^\omega_\alpha\right]\frac{j_2(kr)}{(kr)^2}\right\}, \tag{25}$$

$$m_\alpha = \frac{3}{2}\int \mathrm{d}^3\mathbf{r}\,\left(\mathbf{r}\times\mathbf{J}_\omega\right)_\alpha \frac{j_1(kr)}{kr}, \tag{26}$$

$$\begin{aligned} Q^e_{\alpha\beta} = -\frac{3}{\mathrm{i}\omega}\Bigg\{ &\int \mathrm{d}^3\mathbf{r}\,\left[3\left(r_\beta J^\omega_\alpha + r_\alpha J^\omega_\beta\right) - 2(\mathbf{r}\cdot\mathbf{J}_\omega)\,\delta_{\alpha\beta}\right]\frac{j_1(kr)}{kr} \\ &+ 2k^2\int \mathrm{d}^3\mathbf{r}\,\left[5r_\alpha r_\beta(\mathbf{r}\cdot\mathbf{J}_\omega) - \left(r_\alpha J^\omega_\beta + r_\beta J^\omega_\alpha\right)r^2 - r^2(\mathbf{r}\cdot\mathbf{J}_\omega)\,\delta_{\alpha\beta}\right]\frac{j_3(kr)}{(kr)^3}\Bigg\}, \end{aligned} \tag{27}$$

$$Q^m_{\alpha\beta} = 15\int \mathrm{d}^3\mathbf{r}\,\left\{r_\alpha\,(\mathbf{r}\times\mathbf{J}_\omega)_\beta + r_\beta\,(\mathbf{r}\times\mathbf{J}_\omega)_\alpha\right\}\frac{j_2(kr)}{(kr)^2}. \tag{28}$$

Here $\mathbf{J}_\omega(\mathbf{r}) = \mathrm{i}\omega\varepsilon_0(\varepsilon_r - 1)\mathbf{E}_\omega(\mathbf{r})$, where $\mathbf{E}_\omega(r)$ is the electric field distribution, $\varepsilon_0$ is the permittivity of free space, $\varepsilon_r$ is the permittivity of the Au helicoid, $j_n(kr)$ are spherical Bessel functions of order $n$ and $\alpha$,$\beta = x$,$y$,$z$.

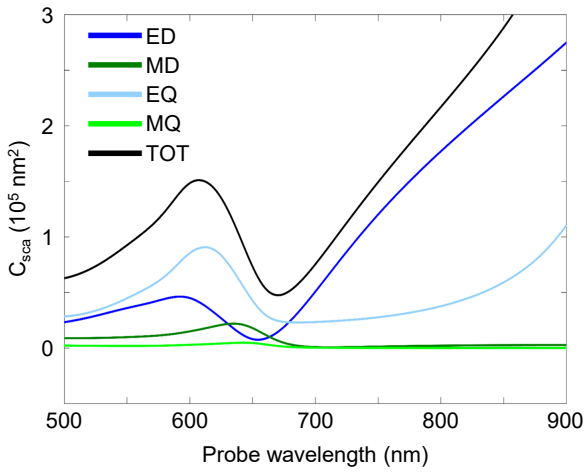


**Fig. S5 Multipolar decomposition.** Static scattering cross-sections of individual multipole moments and total contribution.

From the multipole moments, the corresponding scattering cross-sections (shown in Fig. S5) can be evaluated as follows [4]:

$$
\begin{aligned}
C_{\mathrm{sca}}^{\mathrm{total}} &= C_{\mathrm{sca}}^{p} + C_{\mathrm{sca}}^{m} + C_{\mathrm{sca}}^{Q^e} + C_{\mathrm{sca}}^{Q^m} \\
&= \frac{k^4}{6\pi\,\varepsilon_m^2\,|\mathbf{E}_{\mathrm{inc}}|^2}\left[\sum_{\alpha}\left(|p_\alpha|^2 + \frac{|m_\alpha|^2}{c^2}\right) + \frac{1}{120}\sum_{\alpha\beta}\left(\left|k\,Q^e_{\alpha\beta}\right|^2 + \left|\frac{k\,Q^m_{\alpha\beta}}{c}\right|^2\right)\right],
\end{aligned}
\tag{29}
$$

where $\varepsilon_m$ is the permittivity of the environment. From the multipolar decomposition of the helicoid response, we notice that the scattering associated to the MD moment presents a peak at the same wavelength as the negative dip in the static CD spectrum. This suggests that the feature observed in the CD originates from the interaction between electric and magnetic dipole moments. Conversely, at longer wavelengths, the magnetic dipole vanishes, thus the CD positive peak in this spectral region can only be ascribed to the interaction between electric dipole and quadrupole moments [5]. Moreover, the nano-helicoid MD can be further elucidated by inspecting the spatial distribution of the induced electric charges on the nanoparticle surface, shown in Fig. S6 for both LCP and RCP illumination. Across the chiral gaps (i.e. the concave regions) of the nanostructure, opposite charges provide an effective capacitative coupling, similar to what observed in split-ring resonators, which in turn generates a strong magnetic dipole moment [6].

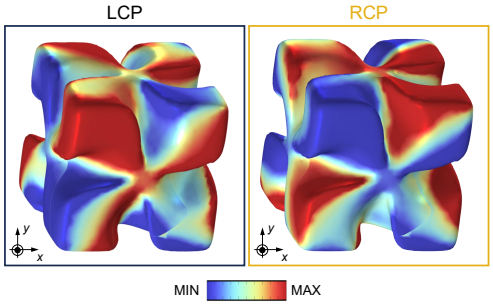


**Fig. S6 Electric charge density.** Simulated charge density of the helicoid under LCP and RCP illumination.

# Supplementary Note 5: Jones calculus for extracting CD and ORD

We start by recasting the Jones matrix of Eq. (10) on a circular basis via the matrix $C$ (defined according to the polarization handedness convention shown in Fig. S1):

$$
\begin{aligned}
M_{\mathrm{chi}}^{C} &= C^{-1} M_{\mathrm{chi}} C = \begin{bmatrix} t_{LL} & t_{LR} \\ t_{RL} & t_{RR} \end{bmatrix} = \\
&= 10^{-\alpha/2} \mathrm{e}^{-\mathrm{i}\rho} \begin{bmatrix} 1 & \mathrm{i} \\ 1 & -\mathrm{i} \end{bmatrix} \begin{bmatrix} 1 & \mathrm{ORD} - \mathrm{iCD} \\ -\mathrm{ORD} + \mathrm{iCD} & 1 \end{bmatrix} \begin{bmatrix} 1 & 1 \\ -\mathrm{i} & \mathrm{i} \end{bmatrix} = \\
&\propto \begin{bmatrix} 1 - \mathrm{iORD} - \mathrm{CD} & 0 \\ 0 & 1 + \mathrm{iORD} + \mathrm{CD} \end{bmatrix}.
\end{aligned} \tag{30}
$$

A simple manipulation of the diagonal elements leads to:

$$
\mathrm{CD} = -\operatorname{Re}\left(\frac{t_{LL} - t_{RR}}{t_{LL} + t_{RR}}\right), \qquad \mathrm{ORD} = -\operatorname{Im}\left(\frac{t_{LL} - t_{RR}}{t_{LL} + t_{RR}}\right). \tag{31}
$$

Furthermore, it is possible to show that the usual definition of CD as a difference of left and right absorbances is consistent with these expressions. Indeed, the transmission $T_L$ and $T_R$ of left- and right-polarized light are

$$
\begin{aligned}
T_L &:= |t_{LL}|^2 = 10^{-\alpha} \left[(1 - \mathrm{CD})^2 + (\mathrm{ORD})^2\right], \\
T_R &:= |t_{RR}|^2 = 10^{-\alpha} \left[(1 + \mathrm{CD})^2 + (\mathrm{ORD})^2\right].
\end{aligned}
$$

Thus, it follows that

$$
\mathrm{CD} = -\frac{1}{2} \frac{T_L - T_R}{T_R + T_L}.
$$

It is possible to apply Lambert-Beer's law ($I_{L,R} = I_0 e^{-\alpha_{L,R} \ln 10}$) to express $T_L$, $T_R$ in terms of the absorbances $\alpha_L$, $\alpha_R$: $T_{L,R} = I_{L,R}/I_0 = e^{-\alpha_{L,R} \ln 10}$. Then, by defining $\Delta\alpha = \alpha_L - \alpha_R$,

$$
\mathrm{CD} = -\frac{1}{2} \left( \frac{e^{-\alpha_L \ln 10} - e^{-\alpha_R \ln 10}}{e^{-\alpha_L \ln 10} + e^{-\alpha_R \ln 10}} \right) = -\frac{1}{2} \left( \frac{e^{-\Delta\alpha \ln 10} - 1}{e^{-\Delta\alpha \ln 10} + 1} \right). \tag{32}
$$

Finally, in the small dichroism approximation ($\Delta\alpha << 1$), CD can be expressed as:

$$
\mathrm{CD} = \frac{\ln(10)}{4} (\alpha_L - \alpha_R), \tag{33}
$$

which is Eq. (6).

## Supplementary Note 6: Disentangling the transient chiro-optical response of plasmonic helicoids

The Inhomogeneous Three-Temperature Model (I3TM) [7, 8] introduced in the main text, Eqs. (3)-(5), provides a thermodynamics-inspired description of the non-equilibrium dynamics of plasmonic nanostructures following excitation with ultrashort light pulses. By solving the three coupled partial differential equations formulated for $N$ (the energy density stored in a sub-population of nonthermalised carriers), $\Theta_E$ (the temperature of thermalised carriers), and $\Theta_L$ (the metal lattice temperature), one

could track the temporal flow of excess energy delivered by the pump photons. For the plasmonic nano-helicoids under investigation, the solution of the 3TM is reported in Fig. S7, space-averaged over the volume of the helicoid.

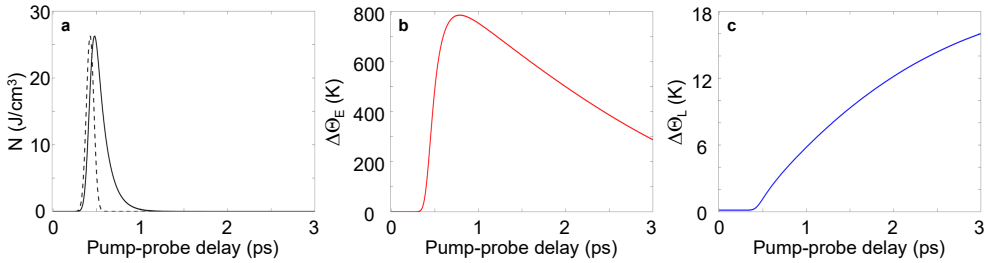


**Fig. S7 Integration of the Three-Temperature Model. a - c.** Temporal dynamics of the plasmonic internal degrees of freedom solved for in the I3TM, averaged over the nano-helicoid volume, namely the average energy density stored in a sub-population of nonthermalised carriers $N$ (**a**), the average electronic temperature $\Theta_E$ (**b**), and the average lattice temperature $\Theta_L$ (**c**). In panel **a**, the (normalised) temporal envelope of the pump pulse, acting as source term of the I3TM is also shown (dotted line).

As formally expressed by Eq. (3) in the main text, the optical excitation (whose normalised temporal evolution is shown as a dotted line in Fig. S7a) is directly coupled to nonthermal electrons (Fig. S7a), which feature an ultrafast rise time and relax back to equilibrium within a few hundred femtoseconds (fully accomplished within 1 ps). Thermalised electrons, described by their temperature $\Theta_E$, which fully determines their Fermi-Dirac-like energy occupancy distribution, exhibit a delayed onset due to electron-electron scattering, and decay within tens of picoseconds while equilibrating with the lattice (Fig. S7b). Finally, on longer timescales, the metal lattice temperature increases (Fig. S7c), albeit only by a few tens of degrees, consistent with the relatively low pump fluences used in the experiments ($300\,\mu J/cm^2$). For the present nanostructure, adopting a homogeneous formulation of the 3TM does not lead to major changes in the overall dynamics of the three variables. This is consistent with the fact that, although the nano-helicoid supports strong electromagnetic hot spots, it retains a compact shape at the nanoscale that limits gradient-driven mechanisms. Importantly, however, the I3TM enables accurate treatment of the complex absorption pattern of the pump pulse within the nanostructure volume, and provides a straightforward way to incorporate the helicity-dependent interaction with the probe beam.

Once the (electronic and optical) effects induced by the pump pulse in the plasmonic nanostructure have been estimated, we numerically assessed the transient changes in the nano-helicoid chiro-optical response. To build the differential maps of $\Delta$CD and $\Delta$ORD (Fig. 3 in the main text), we solved Maxwell's equations (see Methods in the main text) for both left- or right-circularly polarized probe beams as a function of pump-probe time delay and probe wavelength, and suitably combined the obtained transmission coefficients (refer to Eqs. (1)-(2) from the main text). Figure

S8 shows the maps of differential transmission ΔT/T simulated for the two distinct, LCP (Fig. S8a) and RCP (Fig. S8b), polarization states of the incoming probe, following excitation with the same pump pulse. Although the overall temporal dynamics are similar for the two polarization states, the maps reveal differences in terms of both signal amplitude and spectral features, which give rise to the observed transient chiro-optical response.

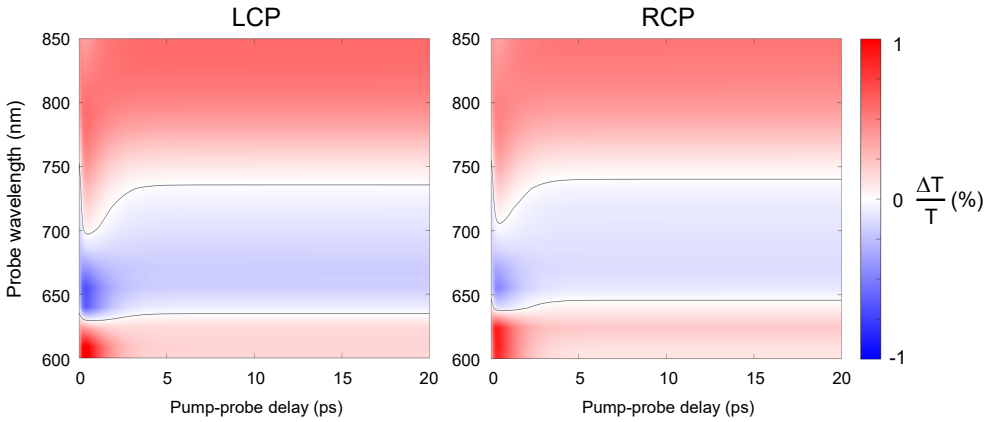


**Fig. S8 Simulated helicity-resolved differential transmission. a - b** Maps of the simulated differential transmission ΔT/T of the plasmonic nano-helicoid array, for a probe beam either left- (**a**, LCP) or right-circularly polarized (**b**, RCP). The simulations are performed considering the same parameters used for the numerical analysis presented in the main text.

Employing the 3TM to describe the non-equilibrium dynamics of the plasmonic nanostructures under study enabled us to disentangle the contributions to the transient chiro-optical response arising from distinct, hot-carrier- and lattice-driven optical nonlinearities. Figure S9 reports the simulated maps (identical to those shown in Fig. 3 of the main text) of the total ΔCD (Fig. S9a) and ΔORD (Fig. S9e), together with the transient CD and ORD obtained by selectively including the nonlinear optical modulations only from non-thermalised carriers (Figs. S9b, S9f), thermalised carriers (Figs. S9c, S9g), and the lattice temperature increase (Figs. S9d, S9h). Notably, this disentangled analysis rationalises the peculiar ultrafast double sign change of the ΔCD observed at 681 nm (refer to Figs. 4g and 4c in the main text). By comparing the ΔCD associated with the three variables $N$, $\Theta_E$, and $\Theta_L$, it is evident that, in selected spectral windows, their contributions may have opposite signs.

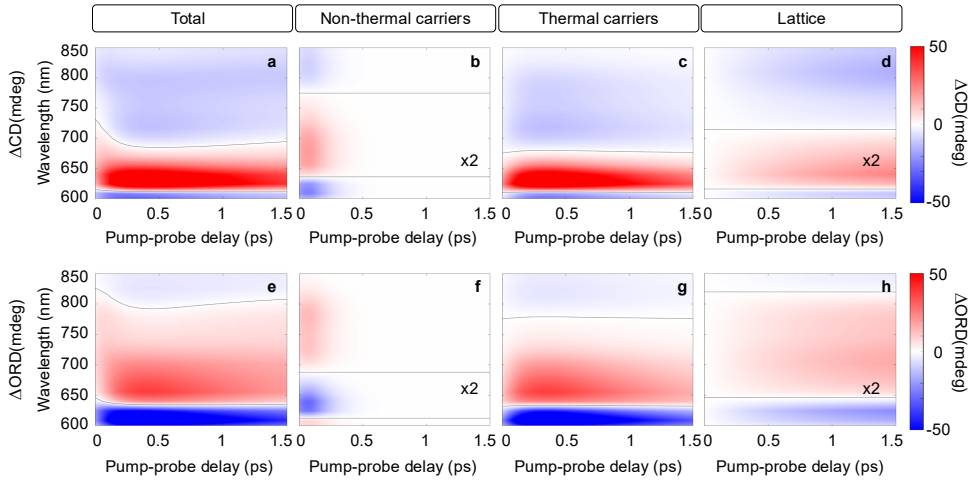


**Fig. S9 Disentangling the transient chiro-optical response of plasmonic helicoids. a - d.** Simulated map of the ultrafast ΔCD (**a**) as a function of the probe wavelength and pump-probe delay, disentangled in the contributions arising from non-thermalised carriers (**b**, magnified by a factor of 2 for better reading), thermalised carriers (**c**), and the metal lattice (**d**, magnified by a factor of 2 for better reading), respectively. **e - h**, Same as (**a - d**), for the ultrafast ΔORD.

Specifically, in the range between ∼670 nm and ∼760 nm, non-thermalised carriers produce a positive modulation of the CD that vanishes within a few hundred femtoseconds, while the increased electronic temperature induces a negative ΔCD. The lattice temperature contribution, in turn, switches sign from positive to negative around 710 nm, with a delayed onset governed by electron-phonon scattering. These distinctive spectro-temporal signatures provide the precise explanation for the two sign inversions of the total ΔCD recorded at 681 nm: a positive-to-negative sign switch at early time delays, followed by the reverse after ∼1 ps, arising indeed from the dynamical interplay of the three contributions.

Finally, we carried out a multipolar decomposition analysis in the out-of-equilibrium regime to numerically examine the role of the electric-magnetic dipole interaction in shaping the transient CD. To this end, we extended the static model described in Supplementary Note 4 by incorporating the pump-induced time-dependent permittivity of the helicoid. This was achieved by adapting the I3TM introduced in the main text to the case of a single scatterer, which required recasting the driving term $P_{\mathrm{abs}}$, following previous reports [9]. The contribution of the interaction between the electric and magnetic dipole moments to the CD can be related to the imaginary part of their in-plane scalar product [10], $\mathrm{Im}\left[\mathbf{p}\cdot\mathbf{m}\right]_{xy}$. We therefore tracked the non-equilibrium dynamics of this quantity, and its spectral variations over

time, as reported in Fig. S10 for selected pump-probe delays. The calculated differential spectra closely resemble those of the ΔCD (refer to Fig. 3 of the main text), with a dominant positive peak around 630 nm and two weaker negative lobes at shorter and longer wavelengths. For the latter ($\lambda >\sim 660$ nm), the agreement with the ΔCD is slightly reduced, possibly because of other multipolar interactions becoming significant in this spectral region. Notably, the temporal dynamics of $\Delta\Big(\mathrm{Im}\left[\mathbf{p}\cdot\mathbf{m}\right]_{xy}\Big)$ also qualitatively matches that of the observed ΔCD, with both signals exhibiting comparable rise and decay rates (compare traces in Fig. S10 and in Fig. 4 of the main text).

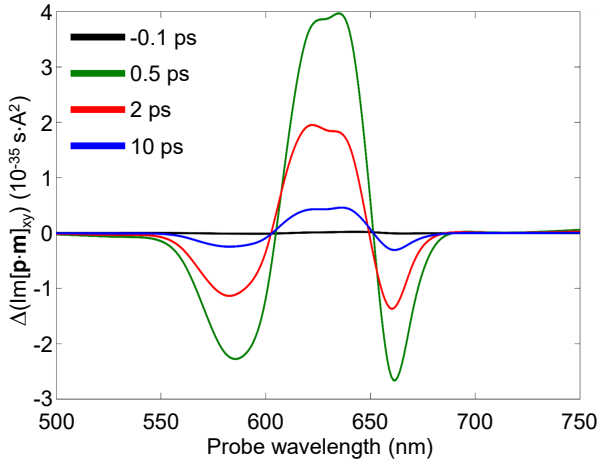


**Fig. S10 Electric-magnetic dipole interaction.** Simulated spectra of the differential imaginary part of the scalar product between electric and magnetic dipole at different pump-probe delays.

## Supplementary Note 7: Spin thermalization in lead halide perovskite

Figure 5 of the main text depicts spin-selective excitation of carriers by means of circularly polarized light pulses in a lead mixed-halide perovskite. The initial red-shift of the CD peak has been attributed to the cooling of the spin population (see Fig. 5c) [11]. Due to the Kramers-Kronig relation connecting CD and ORD, the cooling of spin polarized carriers manifests itself in the ΔORD map as well, as a shift of the isosbestic line (see Fig. S11a). Building on this, we extract the characteristic time by fitting the progressive redshift of the isosbestic point with a mono-exponential function, finding a value $\tau_c = 300$ fs (see Fig. S11b). On the other hand, the decay of the trCD trace is attributed to spin depolarization mechanisms, as reported in the main text. Fig. S12 shows the dynamics of at the peak of the trCD signal, together with a biexponential fitting, where the two time constants (namely a fast one, $\tau_h$ and a slow one, $\tau_e$) are representative of the typical hole and electron depolarization times.

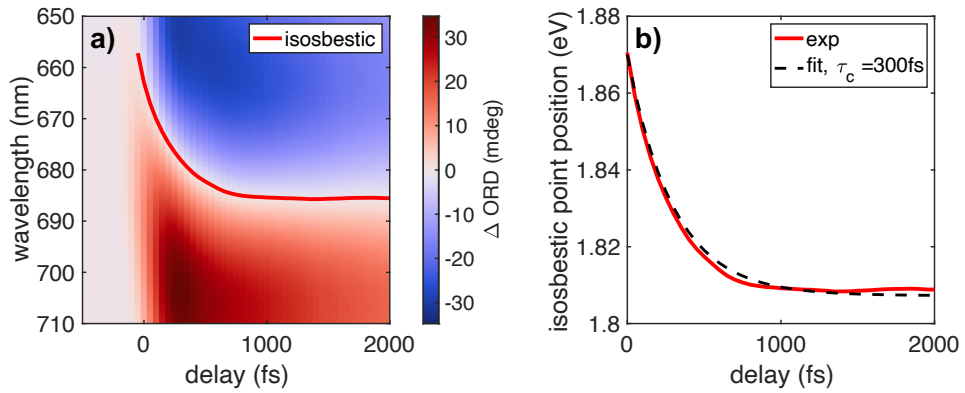


**Fig. S11 Extrapolation of the spin thermalization time from broadband ORD measurements a.** Broadband trORD map of the lead halide perovskite excited by $\sigma^+$ pulses at 515 nm. The delay-dependent position of the isosbestic point is indicated by the red line **b.** Temporal evolution of the isosbestic point, compared to the least squares fit with a single exponential decay.

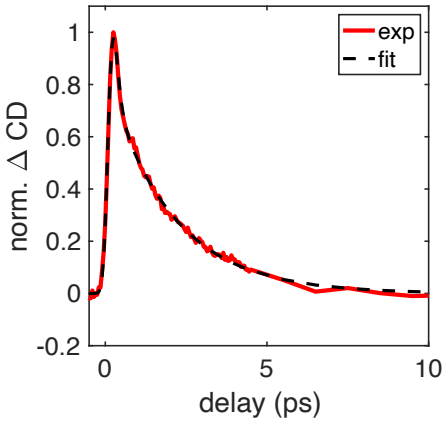


**Fig. S12 Extrapolation of the spin depolarization time from broadband CD measure.** Red line: trCD trace, normalized and integrated over the whole probe wavelength range. Black line: biexponential fitting, where $\tau_h = 110$ fs (resolution limited), $\tau_e = 2000$fs.

# References


[1] Lindell, I. V. (ed.) *Electromagnetic waves in chiral and bi-isotropic media* The Artech House antenna library (Artech House, Boston, 1994).

[2] Barron, L. D. *Molecular Light Scattering and Optical Activity* 2nd edn (Cambridge University Press, Cambridge, 2004).

[3] Lininger, A. *et al.* Chirality in Light–Matter Interaction. *Advanced Materials* **35**, 2107325 (2023).

[4] Alaee, R., Rockstuhl, C. & Fernandez-Corbaton, I. An electromagnetic multipole expansion beyond the long-wavelength approximation. *Optics Communications* **407**, 17–21 (2018).

[5] Kim, J. W. *et al.* Controlling the size and circular dichroism of chiral gold helicoids. *Materials Advances* **2**, 6988–6995 (2021).

[6] Ahn, H.-Y. *et al.* Highly chiral light emission using plasmonic helicoid nanoparticles. *Adv. Opt. Mater.* **12**, 2400699 (2024).

[7] Sun, C.-K., Vallée, F., Acioli, L. H., Ippen, E. P. & Fujimoto, J. G. Femtosecond-tunable measurement of electron thermalization in gold. *Phys. Rev. B* **50**, 15337–15348 (1994).

[8] Schirato, A., Maiuri, M., Cerullo, G. & Della Valle, G. Ultrafast hot electron dynamics in plasmonic nanostructures: experiments, modelling, design. *Nanophotonics* **12**, 1–28 (2023).

[9] Schirato, A. *et al.* Pump-selective spectral shaping of the ultrafast response in plasmonic nanostars. *J. Phys. Chem. C* **128**, 2551–2560 (2024).

[10] Zhu, A. Y. *et al.* Giant intrinsic chiro-optical activity in planar dielectric nanostructures. *Light Sci. Appl.* **7**, 17158 (2017).

[11] Giovanni, D. *et al.* Ultrafast long-range spin-funneling in solution-processed Ruddlesden–Popper halide perovskites. *Nat. Commun.* **10**, 3456 (2019).